# Voronoi neighbor statistics of homogeneously sheared inelastic hard disks and hard spheres

V. Senthil Kumar and V. Kumaran
*Department of Chemical Engineering, Indian Institute of Science, Bangalore 560 012, India*
(Received 28 November 2005; published 19 May 2006)

In this work we extend our earlier Voronoi neighbor analysis [J. Chem. Phys. **123**, 074502 (2005)] to homogeneously sheared inelastic hard-particle structures, the simplest model for rapid granular matter. The pair distribution function is partitioned into the $n$th neighbor coordination number ($C_n$), and the $n$th neighbor position distribution [$f_n(\mathbf{r})$]. The distribution of the number of Voronoi faces ($P_n$) is also considered since $C_1$ is its mean. We report the $C_n$ and $P_n$ for the homogeneously sheared inelastic hard-disk and hard-sphere structures. These statistics are sensitive to shear ordering transition, the nonequilibrium analogue of the freezing transition. In the near-elastic limit, the sheared fluid statistics approach that of the thermodynamic fluid. On shear ordering, due to the onset of order, the $C_n$ for sheared structures approach that of the thermodynamic solid phase. The suppression of nucleation by the homogeneous shear is evident in these statistics. As inelasticity increases, the shear ordering packing fraction increases. Due to the topological instability of the isotropically perturbed face-centered cubic lattice, polyhedra with faces 12 to 18, with a mean at 14, coexist even in the regular close packed limit for the thermodynamic hard-sphere solid. In shear ordered inelastic hard-sphere structures there is a high incidence of 14-faceted polyhedra and a consequent depletion of polyhedra with faces 12, 13, 15–18, due to the formation of body-centered-tetragonal (bct) structures. These bct structures leave a body-centered-cubic-like signature in the $C_n$ and $P_n$ data. On shear ordering, close-packed layers slide past each other. However, with a velocity-dependent coefficient of restitution, at a critical shear rate these layers get disordered or amorphized. We find that the critical shear rate for amorphization is inversely proportional to the particle diameter, as compared to the inverse square scaling observed in dense colloidal suspensions.

DOI: 10.1103/PhysRevE.73.051305 PACS number(s): 45.05.+x, 47.70.−n

## I. INTRODUCTION

The Voronoi polyhedron of a nucleus point in space is the innermost polyhedron formed by the perpendicularly bisecting planes between the given nucleus and all the other nuclei [1]. The Voronoi tessellation divides a region into space filling, nonoverlapping convex polyhedra. The salient properties of Voronoi tessellation are the following.

Any point inside a Voronoi cell is closer to its nucleus than any other nuclei, Fig. 1. These cells are space filling and hence a precise definition of local volume [2].

It gives a definition of geometric neighbors. The nuclei sharing a common Voronoi surface are geometric neighbors. Points on the shared surface are equidistant to the corresponding pair of nuclei. Hence geometric neighbors are competing centers in a growth scenario.

Voronoi cells of hard spheres are irregular at lower packing fractions, but become regular as the regular close packing is approached. Thus, they are useful is characterizing all structures, from random to regular.

These properties qualify Voronoi tessellation as an important tool in the structural analysis of random media such as glass, packings, foams, cellular solids, proteins, etc. [3–5]. Voronoi tessellation occurs naturally in growth processes such as crystallization and plant cell growth [6], It is used (and even rediscovered under different names) in various fields such as meteorology, geology, ecology, metallography, archeology, etc. The statistical distributions of many Voronoi cell properties are reported, see Zhu *et al.* [7], Oger *et al.* [8], and references therein. In an earlier work [9], we presented the Voronoi neighbor analysis for thermodynamic and quenched structures. Here, we extend the analysis to homogeneously sheared hard-disk and hard-sphere structures, and compare them with the thermodynamic hard structures.

We have generated the thermodynamic hard structures using the canonical Monte Carlo (NVE-MC) method, and the homogeneously sheared inelastic hard structures using the Lees-Edwards boundary conditions [10,11], outlined in Sec. II. Inelastic hard particles are the simplest model for rapid granular matter. In most of the work, we use the constant coefficient of restitution (COR) model for inelastic collisions. Due to a lack of an intrinsic energy scale, these structures are shear rate independent. Hence, to study the effect of shear rate on structures we use a velocity-dependent

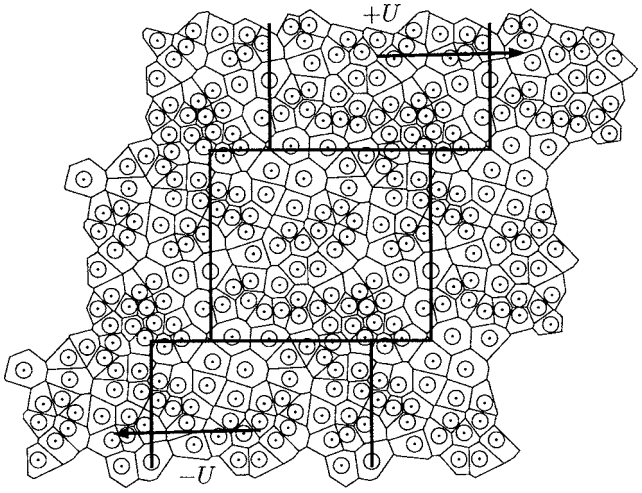


FIG. 1. A configuration with Lees-Edwards boundary condition and Voronoi tessellation, with periodic boundary conditions (PBCs).

 

COR. We propose a functional form for the velocity-dependent COR, which accommodates all the known theoretical scalings.

In Sec. III we introduce the Voronoi neighbor statistics. Let a central sphere's geometric neighbors be called first neighbors, i.e., the first layer of neighbors. The first neighbors' neighbors (which are themselves not first neighbors) are the second neighbors, and so on. Thus, all the spheres surrounding a central sphere are partitioned layerwise, and characterized by $n$th neighbor coordination number ($C_n$) and $n$th neighbor position distribution function [$f_n(\mathbf{r})$]. In Sec. III we show that the total information contained in the pair distribution function $g(\mathbf{r})$ can be partitioned into these sets of neighbor statistics. The distribution of the number of Voronoi bounding surfaces ($P_n$) is also of interest, since $C_1$ is its mean. These neighbor statistics are sensitive to the shear ordering transition. In this work, the usage shear ordering is exclusively used for that nonequilibrium structural transition which approaches the thermodynamic ordering or freezing transition, in the near-elastic limit. We avoid the usage shear-induced ordering, since homogeneous shear in fact suppresses the crystallite nucleation, as discussed below.

In Secs. IV and V we present the $C_n$ and $P_n$ for sheared inelastic hard-disk and hard-sphere structures, respectively. In the near-elastic limit the sheared fluid statistics approach that of the thermodynamic fluid values. When the sheared neighbor statistics approach the thermodynamic solid phase values, shear ordering transition takes place. On shear ordering, close packed strings of hard disks slide over each other in the velocity direction, as observed in the sheared monolayer experiments of Stancik *et al.* [12]. The dislocations in a crystalline solid do not move with the same degree of ease along different crystallographic planes. Generally there are preferred crystallographic planes called the "slip planes," and the preferred directions lying in those planes are called the "slip directions." For the face-centered-cubic (fcc) lattice, the $\{111\}$ family of planes are the slip planes and the $\langle 110\rangle$ directions are the slip directions. A slip plane and a slip direction constitute a slip system. Materials plastically deform by slipping along a slip system [13]. In dense sheared hard-sphere simulations, having an fcc lattice as the initial configuration, an orientation is said to be "preferred" if the velocity-vorticity plane and the velocity vector form a slip system, any other orientation is said to be "unpreferred." In the preferred orientation shear of inelastic hard spheres, on shear ordering, close packed two-dimensional layers of spheres slide over each other in a zig-zag path, as observed in plastic deformation of fcc crystals [14] and colloidal suspensions [15]. In colloids and dense suspensions, such a layerwise flow causes shear thinning, since sliding close-packed layers offer lesser resistance to shear than a disordered structure [16]. The Voronoi statistics clearly show the suppression of crystal nucleation by homogeneous shear, observed in the Brownian dynamics simulations of colloidal suspensions by Butler and Harrowell [17] and Blaak *et al.* [18]. However, in some experiments it is observed that the in-plane ordering. caused by shear, increases the nucleation, see the references in Ref. [18].

For a perfect fcc lattice $C_1=12$, since the unit cell is a rhombic dodecahedron. However, an isotropically perturbed fcc lattice has polyhedra with faces 12 to 18, with a mean at 14, due to a topological instability discovered by Troadec *et al.* [19], we have outlined the original proof in the appendix of Ref. [9]. In shear ordered inelastic hard-sphere structures there is a high incidence of 14-faceted polyhedra and a consequent depletion of polyhedra with faces 12, 13, 15–18. This shows the presence of a nearly body-centered-cubic structure, since the Voronoi polyhedron of the body-centered-cubic (bcc) lattice is the truncated octahedron, which has 14 faces. It is known that in the martensitic transformations, a rapidly quenched fcc metallic structure gets sheared to the body-centered-tetragonal (bct) structure [13]. The bct structures generated in a dense system of homogeneously sheared inelastic hard spheres leave a bcc-like signature in the $C_n$ and $P_n$ data.

In an unpreferred orientation shear of inelastic hard spheres, at packing fractions above shear ordering, the structures get disordered or amorphized. Such a metastable amorphization is observed by Ikeda *et al.* [20] in the unpreferred orientation shear of nanocrystals. This is a metastable amorphization, since the system will eventually recrystallize in the preferred orientation. When the imposed displacement or velocity does not lie on a slip plane, simultaneous slip and shear can break the lattice. We consider this to be the cause of amorphization in an unpreferred orientation shear. These amorphized structures are nearly identical to the dense random structures, except for the higher incidence of some high-faceted polyhedra at the expense of some low-faceted ones. This can be rectified by a structural relaxation using the Monte Carlo based swelled random algorithm [9]. Thus, the Lees-Edwards boundary condition simulation for nearly elastic hard spheres sheared in an unpreferred orientation, followed by a structural relaxation using the swelled random algorithm, offers a nearly deterministic algorithm to generate dense random packings.

A steady state amorphization is the cause of shear thickening observed in dense suspensions [21,22]. The constant COR sheared structures are shear rate independent, hence they cannot amorphize as shear rate is varied. We show that, with a velocity-dependent COR, steady state amorphization is achieved even in the preferred orientation. Even when the system is globally in the preferred orientation, the slip planes are locally misoriented near edge dislocations and grain boundaries. At these locations, shear induces local amorphization, since velocity does not lie on these local slip planes. When the local amorphization rate exceeds the local recrystallization rate, a steady amorphized state results. We observe that the critical shear rate for amorphization is inversely proportional to the sphere diameter, as predicted by Savage and Jeffreys [23] for granular suspensions, unlike the inverse square scaling observed in the colloidal suspensions [21,22].

## II. HOMOGENEOUSLY SHEARED INELASTIC HARD STRUCTURES

We generate homogeneously sheared inelastic hard-particle configurations, Fig. 1, using the Lees-Edwards boundary conditions [10], an event-driven nonequilibrium

molecular dynamics algorithm. The simulation box dimensions are $l_x$, $l_y$, and $l_z$. In our simulation geometry, $x$, $y$, and $z$ are the velocity, gradient, and vorticity directions, respectively. In two-dimensional simulations, the $z$ direction is absent. The top and the bottom boxes move with velocities $+U$ and $-U$, respectively, with respect to the central box. When a particle crosses the top/bottom boundary of the central box with a horizontal velocity $v_x$, its image enters through the bottom/top with a horizontal velocity $(v_x)_{\text{image}}=v_x \mp U$. This induces shear at the top/bottom boundaries of the central box, which then propagates by collisions into the central box. The post-collisional velocity $\mathbf{u}'$ of the smooth particles of identical mass undergoing a binary collision is given in terms of the precollisional velocities as

$$\mathbf{u}_1' = \mathbf{u}_1 - \frac{1+\epsilon}{2}(\mathbf{w}\cdot\mathbf{k})\mathbf{k},$$

$$\mathbf{u}_2' = \mathbf{u}_2 + \frac{1+\epsilon}{2}(\mathbf{w}\cdot\mathbf{k})\mathbf{k},$$

where $\mathbf{w}=\mathbf{u}_1-\mathbf{u}_2$, $\mathbf{k}$ is the unit vector along the line joining the centers of the colliding particles 1 and 2, and $\epsilon$ is the coefficient of normal restitution. The energy input to the system due to shear is lost within the system by inelastic collisions, hence a thermostat is not required. When the system is below its shear ordering packing fraction, a linear velocity profile with a shear rate $\dot{\gamma}=U/l_y$ is induced in the central box. Above the shear ordering packing fraction, the close-packed layers slide over each intermittently and a linear velocity profile does not develop, see, for example, Fig. 10 of Ref. [24]. Further details on the inelastic hard-particle implementation of the algorithm are available in Refs. [11,25]. In our simulations the initial state is the hexagonal packing for hard disks and fcc packing for hard spheres. To disintegrate the initial lattice, we allow 100 elastic collisions per particle. Then the collisions are made inelastic, and the granular temperature is monitored. We found that allowing 5000 inelastic collisions per particle is sufficient to reach steady state. We have ensured that our structural statistics are unaffected by the initial lattice by using the swelled random [9] initial configurations.

A real collision is characterized using three coefficients: the normal and tangential coefficients of restitution and a frictional coefficient [26]. For smooth particles, only the normal coefficient of restitution (COR) $\epsilon$, needs to be considered. It is known long since that $\epsilon$ depends on the impact velocity ($v_{\text{im}}$) [27]. The following theoretical results are available in the plastic and viscoelastic limits.

When the impact velocities are comparable to the yield velocity ($v_Y$), due to plastic deformation [28]

$$\epsilon \sim v_{\text{im}}^{-1/4}. \tag{1}$$

Johnson [29] showed that, when $v_{\text{im}} \gg v_Y$,

$$\epsilon \approx 1.18\ (v_{\text{im}}/v_Y)^{-1/4}. \tag{2}$$

This asymptotic result is experimentally observed for Nylon [30] and steel [31]. For the two-dimensional plastic deformation $\epsilon \sim v_{\text{im}}^{1/3}$ [32].

When the impact velocities are much lower than the yield velocity, due to viscoelastic dissipation, $1-\epsilon \sim v_{\text{im}}^{1/5}$ [33]. Schwager and Poschel [34,35] have shown that, when $v_{\text{im}} \ll v_Y$,

$$\epsilon = 1 - \gamma_1 v_{\text{im}}^{1/5} + \gamma_2 v_{\text{im}}^{2/5} - \gamma_3 v_{\text{im}}^{3/5} + \cdots, \tag{3}$$

where $\gamma_1$ and $\gamma_2$ are positive material-dependent constants.

The abovementioned are the theoretical results. Now, we take note of the models used in simulations.

A constant COR model is still widely used to acquire insights into the cooperative phenomena in granular matter [36].

There is a step model [37] (reminiscent of the square-well approximation for the Lennard-Jones potential),

$$\epsilon = \begin{cases} 1 & \text{if } v_{\text{im}} \leqslant v_c, \\ \epsilon_c & \text{if } v_{\text{im}} > v_c, \end{cases}$$

where $v_c$ and $\epsilon_c$ are constant cutoff values.

Spahn *et al.* [38] use the form

$$\epsilon = \frac{A}{(A^4 + v_*)^{1/4}}, \tag{4}$$

where $A \approx 0.2-0.4$ is a fit parameter and $v_*=v_{\text{im}}/v_Y$ is the dimensionless impact velocity. This form satisfies $\epsilon \to 1$ when $v_* \approx 0$ and the plastic deformation power dependence [Eq. (1)]. However, it does not accommodate Johnson's asymptotic result [Eq. (2)] and the viscoelastic dissipation power dependence [Eq. (3)].

McNamara and Falcon [39] use the piece-wise model for steel spheres in a vibrated bed

$$\epsilon = \begin{cases} 1-(1-\epsilon_Y)v_*^{1/5} & \text{if } v_{\text{im}} < v_Y, \\ \epsilon_Y v_*^{-1/4} & \text{if } v_{\text{im}} > v_Y, \end{cases}$$

where $\epsilon_Y$ is a fit parameter, and reproduce experimental trends. This form does not accommodate the Johnson's asymptotic result (2), which is observed in the steel COR data, see Fig. 7 of Ref. [31].

We have modified the form of Eq. (4) to accommodate the viscoelastic dissipation [Eq. (3)] as

$$\epsilon = \frac{A + B\exp(-Cv_*^{1/5})}{[(A+B)^4 + v_*]^{1/4}}, \tag{5}$$

with $A=1.18$ to accommodate Johnson's asymptotic result (2), and $B, C$ are fit parameter. This form accommodates the theoretical results Eqs. (1)–(3), and seems to fit well the data for Nylon in Ref. [30] and that for steel in Ref. [31].

In most part of this work, we use a constant COR model, since the resultant sheared structures are shear rate independent, i.e., any nonzero shear rate produces the same structure and a statistical geometric analysis could be carried out with the two parameters: packing fraction $\nu$ and the constant COR $\epsilon$. However, when we need to study the shear rate dependent effects, we use the form Eq. (5), with $B=0.12$ and $C=0.44$, they fit well the experimental data for Nylon spheres reported in Ref. [30], they report $v_Y \approx 9$ m/s.

## III. VORONOI PARTITIONING OF THE PAIR DISTRIBUTION FUNCTION

Let $\bar{v}$ be the average volume per particle and $\rho=1/\bar{v}$ the number density. Then the packing fraction $\nu$ is $\pi\sigma^2/(4\bar{v})$ for hard disks and $\pi\sigma^3/(6\bar{v})$ for hard spheres, where $\sigma$ is the diameter. Let $N_n$ be the number of $n$th neighbors around a central disk, then the $n$th neighbor coordination number is $C_n=\langle N_n\rangle$, where $\langle\cdots\rangle$ denotes time averaging. The two-dimensional (in the most general case) anisotropic pair distribution function is computed as

$$g(r,\theta)=\frac{\rho(r,\theta)}{\rho}=\frac{1}{\rho}\frac{\langle\delta N_{r,\theta}\rangle}{\delta V_{r,\theta}}, \tag{6}$$

where $\delta V_{r,\theta}$ is the area element $rdrd\theta$ about $(r,\theta)$ and $\delta N_{r,\theta}$ is the number of disks with their centers in that area element. The disks around the central disk can be partitioned layer-wise as

$$\delta N_{r,\theta}=\sum_{n=1}^{\infty}\delta N^n_{r,\theta}, \tag{7}$$

where $\delta N^n_{r,\theta}$ is the number of $n$th neighbors with their centers in the area element $dV_{r,\theta}$. Using Eq. (7) in Eq. (6), $g(r,\theta)$ can be partitioned as

$$g(r,\theta)=\frac{1}{\rho}\sum_{n=1}^{\infty}\frac{\langle\delta N^n_{r,\theta}\rangle}{\delta V_{r,\theta}}=\sum_{n=1}^{\infty}g_n(r,\theta), \tag{8}$$

where $g_n(r,\theta)$ is the $n$th neighbor anisotropic pair distribution function. Such a partitioning for the isotropic fluid was first reported by Rahman [40].

The $n$th neighbor anisotropic position distribution function, $f_n(r,\theta)$, is denned such that $f_n(r,\theta)rdrd\theta$ is the fraction of the $n$th neighbors in the area segment $rdrd\theta$ about $(r,\theta)$. Then

$$f_n(r,\theta)rdrd\theta=\frac{\langle\delta N^n_{r,\theta}\rangle}{\left\langle\int_{r=0}^{\infty}\int_{\theta=0}^{2\pi}\delta N^n_{r,\theta}rdrd\theta\right\rangle}=\frac{\langle\delta N^n_{r,\theta}\rangle}{C_n}. \tag{9}$$

Here, we have used $\langle\int_{r=0}^{\infty}\int_{\theta=0}^{2\pi}\delta N^n_{r,\theta}rdrd\theta\rangle=\langle N_n\rangle=C_n$. Using Eqs. (8) and (9) we get

$$g_n(r,\theta)=\frac{C_n}{\rho}f_n(r,\theta). \tag{10}$$

Here, we have used $\delta V_{r,\theta}=rdrd\theta$. Then

$$g(r,\theta)=\frac{1}{\rho}\sum_{n=1}^{\infty}C_nf_n(r,\theta). \tag{11}$$

The analogous result for three-dimensional anisotropic pair distribution function is

$$g(r,\theta,\phi)=\frac{1}{\rho}\sum_{n=1}^{\infty}C_nf_n(r,\theta,\phi). \tag{12}$$

Here, $f_n(r,\theta,\phi)$ is defined such that $f_n(r,\theta,\phi)r^2\sin\theta drd\theta d\phi$ is the fraction of the $n$th neighbors in the volume element $r^2\sin\theta drd\theta d\phi$ about $(r,\theta,\phi)$, where $0\leqslant\phi<2\pi$ and $0\leqslant\theta\leqslant\pi$. Equations (11) and (12) show that the two Voronoi neighbor statistics $C_n$ and $f_n(\mathbf{r})$ together contain the structural information in the anisotropic pair distribution function $g(\mathbf{r})$. We consider another Voronoi statistic, the distribution of the number of bounding surfaces of the Voronoi cell $P_n$. It is identical to the distribution of the number of the first neighbors, hence $C_1=\Sigma nP_n$. In Secs. IV and V, we show that these neighbor statistics are sensitive indicators of the microstructural changes occurring in sheared hard-disk and hard-sphere structures.

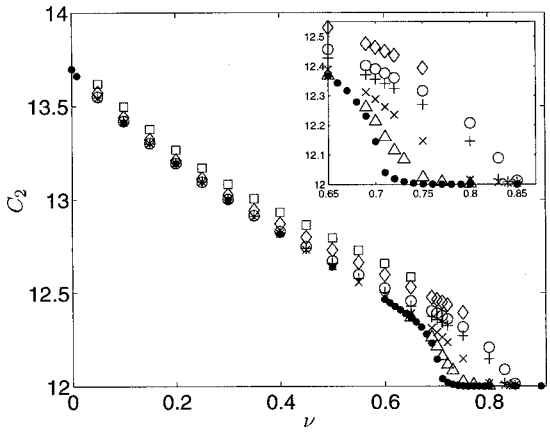


FIG. 2. $C_2$ for sheared inelastic hard-disk structures at $\epsilon=0.50$ (□), 0.70 (◇), 0.90 (○), 0.95 (+), 0.99 (×), and 0.999 (△), compared with NVE structures (•). All data averaged for 10 000 configurations of 256 hard disks, with PBCs.

## IV. HARD-DISK RESULTS

For any nondegenerate two-dimensional tessellation with PBC or with a large number of particles, $C_1=6$ exactly [41,42]. Hence we present the values of $C_2$ and $C_3$ for the entire density range, at different values of $\epsilon$, in Figs. 2 and 3, respectively. From these figures we observe the following.

In the near-elastic limit, the sheared fluid structures are nearly isotropic. Hence the sheared fluid structure $C_n$ (in

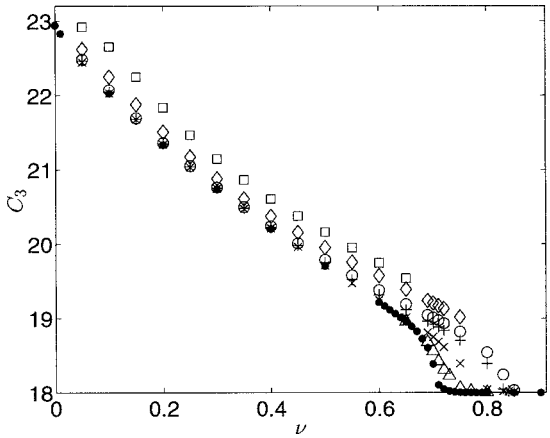


FIG. 3. $C_3$ for sheared inelastic hard-disk structures at $\epsilon=0.50$ (□), 0.70 (◇), 0.90 (○), 0.95 (+), 0.99 (×), and 0.999 (△), compared with NVE structures (•). Averaging as in Fig. 2.

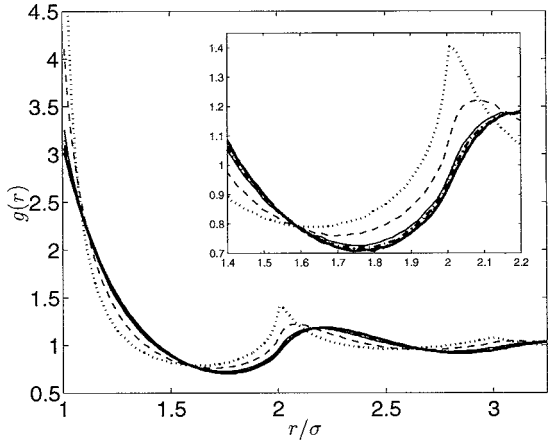


FIG. 4. $g(r)$ at $\nu=0.50$ for sheared inelastic hard-disk structures at $\epsilon=0.50$ (dotted line), 0.70 (thin dashed line), 0.90 (thin line), 0.95 (thick dashed dotted line), and 0.99 (thick dashed line), compared with NVE structure (thick continuous line). The $g(\sigma)$ values are, respectively, about 7.95, 4.40, 3.40, 3.27, 3.17, and 3.10. Averaged over 10 000 configurations of 256 hard disks with PBCs.

Figs. 2 and 3) and the angular-averaged pair distribution function (in Fig. 4)

$$g(r) = \frac{1}{2\pi}\int_{\theta=0}^{2\pi} g(r,\theta)d\theta,$$

approach their respective thermodynamic fluid values. Since the neighbor statistics are by definition angular averaged, the angular-averaged pair distribution function is more appropriate for our analysis than the anisotropic pair distribution function, even though the latter contains the complete structural information.

At packing fractions above the freezing packing fraction ($\nu_F \approx 0.691$ Ref. [43]), the thermodynamic hard disk $C_n$ reduces sharply to its regular hexagonal lattice values $(C_n)_{\text{reg}}=6n$. Above the melting packing fraction ($\nu_M \approx 0.716$, Ref. [43]) the hard-disk system exists as the ordered or solid phase.

When the $C_n$ for sheared structures approach that of the thermodynamic solid phase, shear ordering transition takes place. For example, for $\epsilon=0.99$ the ordering transition occurs near $\nu=0.80$ as signaled in Figs. 2 and 3. This criterion is cross checked with the $g(x,y)$ plots in Fig. 5, for $\nu=0.75$ and $\nu=0.80$. On shear ordering, strings of disks slide over each other along the velocity direction, as shown by the tails of the bright spots in Fig. 5 for $\nu=0.80$. Shear of monolayers of polystyrene spheres suspended at the decane-water interface show that particle strings slide past each other at high shear rates [12]. Thus the $C_n$ are sensitive to both the thermodynamic and shear ordering transitions. The sheared hard-disk $C_n$ show negligible system size dependence, as observed from Table I. Since the $C_n$ are the angular-averaged constituents of $g(r,\theta)$ [Eq. (11)], the former's system size dependence will be comparable, if not less due to the angular averaging, than the latter.

The Brownian dynamics simulations of colloidal suspension by Butler and Harrowell [17] and Blaak *et al.* [18] show

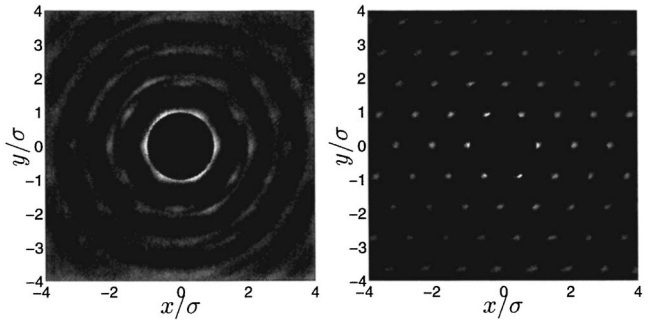


FIG. 5. Pair distribution function for homogeneously sheared inelastic hard disks at $\nu=0.75$ and $\nu=0.80$, at $\epsilon=0.99$. Averaged over 10 000 configurations of 256 hard disks, with PBCs.

that homogeneous shear suppresses the crystal nucleation. In the inset of Fig. 2, note that even though the near-elastic ($\epsilon=0.999$) sheared fluid structure $C_2$ matches with the thermodynamic fluid structure $C_2$ till $\nu_F$, for $\nu > \nu_F$ the $C_2$ for sheared structures drops sluggishly, while the thermodynamic structure $C_2$ drops steeply. This indicates the suppression of crystal nucleation by shear.

TABLE I. System size dependence check for sheared inelastic hard-disk structure $C_2$ and $C_3$, for a constant coefficient of restitution $\epsilon=0.99$.

| $\nu$ | Run | $C_2$ | $C_3$ |
|---|---|---|---|
| 0.70 | I[a] | 12.2883 | 18.7492 |
| | II[b] | 12.2880 | 18.7486 |
| | III[c] | 12.2875 | 18.7483 |
| | IV[d] | 12.2878 | 18.7485 |
| 0.75 | I | 12.1467 | 18.3918 |
| | II | 12.1457 | 18.3895 |
| | III | 12.1534 | 18.4063 |
| | IV | 12.1393 | 18.3666 |
| 0.80 | I | 12.0159 | 18.0431 |
| | II | 12.0279 | 18.0767 |
| | III | 12.0679 | 18.1864 |
| | IV | 12.0614 | 18.1616 |
| 0.83 | I | 12.0067 | 18.0186 |
| | II | 12.0077 | 18.0214 |
| | III | 12.0204 | 18.0581 |
| | IV | 12.0086 | 18.0223 |
| 0.84 | I | 12.0049 | 18.0135 |
| | II | 12.0058 | 18.0161 |
| | III | 12.0051 | 18.0137 |
| | IV | 12.0049 | 18.0126 |

[a]Averaged for 10 000 configurations of 256 hard disks, $l_x:l_y=1:\sqrt{3}/2$.
[b]Averaged for 6400 configurations of 400 hard disks, $l_x:l_y=1:\sqrt{3}/2$.
[c]Averaged for 2850 configurations of 900 hard disks, $l_x:l_y=1:\sqrt{3}/2$.
[d]Averaged for 1600 configurations of 1600 hard disks, $l_x:l_y=1:\sqrt{3}/2$.

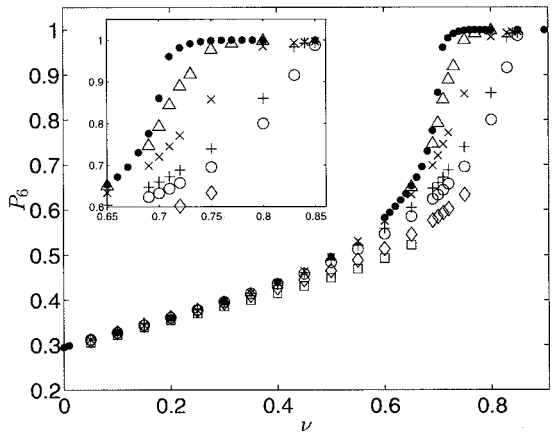


FIG. 6. $P_6$ for sheared inelastic hard-disk structures at $\epsilon$=0.50 (□), 0.70 (◇), 0.90 (○), 0.95 (+), 0.99 (×), and 0.999 (△), compared with NVE structures (•). Averaging as in Fig. 2.

The inset of Fig. 2 shows that as inelasticity increases (i.e., $\epsilon$ decreases) shear ordering occurs at a higher packing fraction. Assuming local equilibrium, this phenomena can be reasoned in analogy with thermodynamic melting as follows: Clausius-Clapeyron equation shows that the melting temperature of a molecular system decreases with decreasing pressure, provided the molar volume of the solid phase is lower than that of the liquid phase and latent heat of fusion is positive. A decrease in melting temperature in a molecular system, translates to an increase in melting density for an athermal system. At a given $\nu$, as inelasticity increases granular pressure decreases. Then, up to an isotropic approximation, fluidity prolongs, i.e., the shear ordering packing fraction increases.

In Figs. 2 and 3, the data for $\epsilon$=0.70 and 0.50 terminate without touching the thermodynamic solid phase due to dynamic inelastic collapse [44]. Dynamic inelastic collapse is a pathological behavior in event-driven simulations where an infinite number of collisions occur in a finite time within clusters, signaled by a sudden drop in collision times and hence negligible evolution of the system in real time. This can be circumvented by inducing a homogeneous density field using impact velocity dependent coefficients of restitution [37]. Even though we simulated such a model to extend the data of $\epsilon$=0.70 and 0.50, we do not present it in Figs. 2 and 3 to maintain the simplicity of two parameter analysis ($\nu$ and $\epsilon$).

It is interesting to note that the trends in $C_2$ and $C_3$ identical, even though they characterize the second and third neighbors, respectively. This shows that Voronoi partitioning is a physically relevant parametrization.

Next, we study the number distribution of the Voronoi polygon edges $P_n$. For two-dimensional configurations with PBC, even though $C_1=\Sigma nP_n=6$ exactly, $P_n$ is a function of density and a sensitive microstructural indicator. We compare the $P_n$ data of the thermodynamic and sheared structures in Figs. 6–8, from which we observe the following.

In two-dimensional systems hexagonal structure is the regular close packing. In thermodynamic structures, across the freezing transition, in response to the onset of order, there is a sharp rise in the hexagon incidence, Fig. 6. Considering

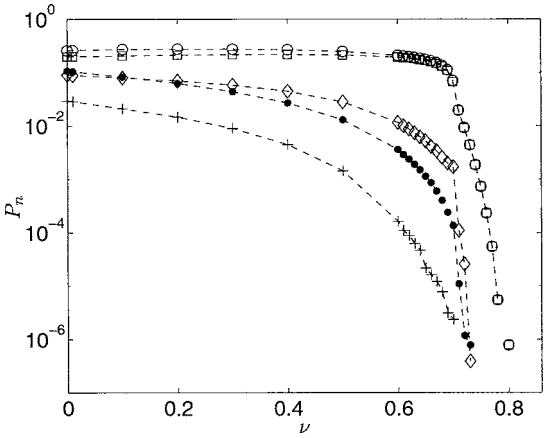


FIG. 7. $P_n$ for hard-disk NVE structures, for $n$=4 (•), 5 (○), 7 (□), 8 (◇), and 9 (+). Averaging as in Fig. 2.

the approach of $P_6$ for sheared structures to that of the thermodynamic structures as the sign of shear ordering leads to conclusions same as before: In the near-elastic limit, the sheared fluid $P_n$ approaches that of the thermodynamic fluid. The suppression of crystal nucleation by shear manifests as the sluggish rise of the near-elastic (for $\epsilon$=0.999) $P_6$ for dense sheared structures ($\nu > \nu_F$), as compared to the steep rise of the thermodynamic $P_6$. As inelasticity increases the shear ordering packing fraction increases.

From Fig. 7 note that in thermodynamic structures, the incidence of polygons with edges 4, 8, and 9 decreases sharply after the freezing transition and the defects in the hard-disk solid structures are represented by nearly identical populations of pentagons and heptagons. Deng *et al.* [45] (and references therein) show that defects in dense two-dimensional systems could be represented by pairs of pentagon and heptagons, and consider them to be a structural dipole. Comparing Figs. 7 and 8, note that the sharp drop in the incidence of polygons with edges 4, 8, and 9 occurs near the shear ordering packing fraction, which is greater than the freezing packing fraction due to inelasticity. The incidence of pentagons and heptagons in dense sheared structures are much greater than those in the dense thermodynamic structures.

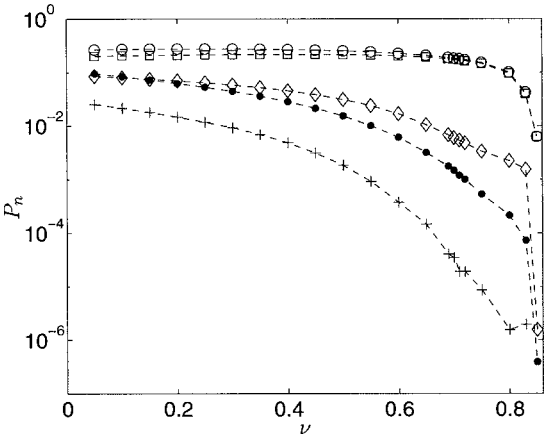


FIG. 8. $P_n$ for sheared inelastic hard-disk structures at $\epsilon$=0.90, for $n$=4 (•), 5 (○), 7 (□), 8 (◇), and 9 (+). Averaging as in Fig. 2.

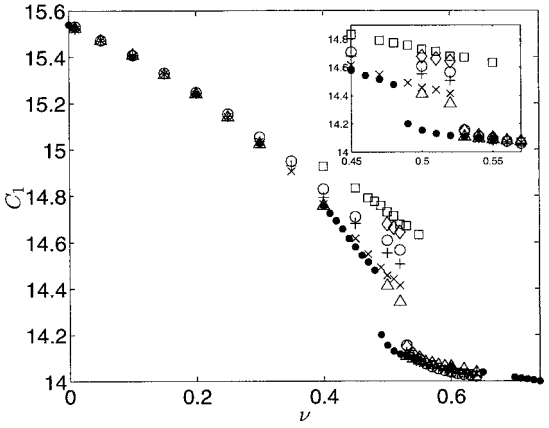


FIG. 9. $C_1$ for inelastic hard-spheres sheared in the preferred orientation, at $\epsilon$=0.70 (□), 0.80 (◇), 0.90 (○), 0.95 (+), 0.99 (×), and 0.999 (△), compared with NVE structures (•). NVE data averaged for 1000 configurations of 256 hard spheres, with PBCs. Sheared structure data averaged for 675 configurations of 384 hard spheres (6 stacks of $8\times8$ hard spheres), with PBC.

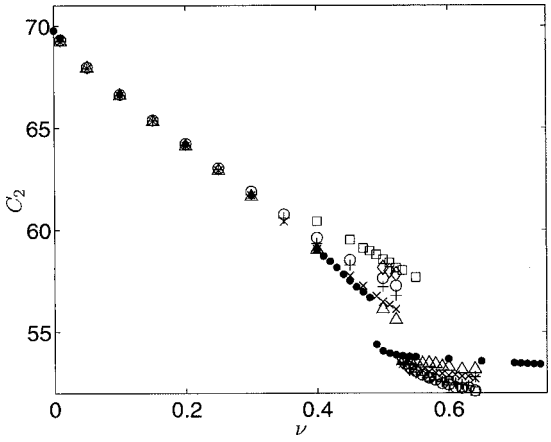


FIG. 10. $C_2$ for inelastic hard-spheres sheared in the preferred orientation, at $\epsilon$=0.70 (□), 0.80 (◇), 0.90 (○), 0.95 (+), 0.99 (×), and 0.999 (△), compared with NVE structures (•). Averaging as in Fig. 9.

The incidence of polygons with edges 3, 10, 11, and 12 decreases sharply with increasing density even for $\nu<\nu_F$ (figure not shown).

## V. HARD-SPHERE RESULTS

Solids with fcc structure undergo plastic deformation by slipping along the ⟨110⟩ directions in the {111} planes [13]. Experimental studies show that in a plane Poiseuille flow of colloidal crystals, the crystals are aligned with their (111) plane parallel to the cell wall and the [110] direction along the velocity [46]. For a recent review on flow-induced structure in colloidal suspensions see Ref. [47]. An orientation in which a {111} plane parallel to the velocity-vorticity ($xz$) plane is the preferred orientation for the shear of fcc lattice, and the other orientations are unpreferred. The usual way of generating the initial fcc configuration for molecular dynamics simulations [48] is an unpreferred orientation, since the (001) plane is parallel to the $xz$ plane. In a sheared fluid state, the orientation of the initial configuration does not matter (shown below). It is known the colloidal solids on shearing in an unpreferred orientation, melt and recrystallize along the preferred orientation. However, this lattice reorientation requires long simulation times. Hence we generate initial configurations in the preferred orientation by stacking layers of two dimensional close-packed spheres in $ABC$ $ABC,\ldots,$order. Suppose we have $p$ stacks (along the $y$ direction) of $q\times q$ spheres forming two-dimensional close-packed spheres (parallel to the $x-z$ plane), then the box relative dimensions are $l_x:l_y:l_z=q:p\sqrt{2}/3:q\sqrt{3}/2$. Figures 9 and 10, respectively, compare the $C_1$ and $C_2$ of inelastic hard spheres sheared in the preferred orientation with those of the thermodynamic structures. From these figures we observe the following.

The $C_n$ are sensitive to thermodynamic freezing and melting transitions. The freezing and melting packing fractions are, respectively, $\nu_F\approx0.494$ and $\nu_M\approx0.545$. Ref. [49]. Fuller [50] derives the expression $C_n=10n^2+2$ for a perfect fcc lattice. $C_1$ for a perfect fcc lattice is 12, since the unit cell is the rhombic dodecahedron. However, due to a topological instability the average number of faces of a Voronoi polyhedron in a perturbed fcc lattice is 14, as shown by Troadec *et al.* [19]. We have outlined the original proof in the appendix of our earlier work Ref. [9]. Thus, the thermodynamic structure $C_1$ approaches 14 instead of 12.

As in the sheared inelastic hard-disk structures, the near-elastic sheared fluid structure $C_n$ are identical to the thermodynamic structure $C_n$.

When the sheared structures undergo the shear ordering transition, the $C_n$ drops close to the thermodynamic solid $C_n$ value. On shear ordering, close-packed two-dimensional layers slide past each other. The shear ordering transition causes shear thinning in colloids and dense suspensions, since layers sliding past each other offer lesser resistance to shear than a disordered structure [16]. The sheared hard sphere $C_n$ show negligible system size dependence, as observed from Table. II.

The near-elastic ($\epsilon$=0.999) $C_n$ drop to the thermodynamic solid phase values at a higher packing fraction than the thermodynamic fluid branch, due to the suppression of crystal nucleation in a homogeneous shear field [18]. For $\epsilon$=0.999, 0.99, 0.95, 0.90, and 0.80, the shear-ordering packing fraction varies within the narrow range of 0.52–0.53. However, for $\epsilon$=0.70 the shear-ordering packing fraction is between 0.54 and 0.55 (inset of Fig. 9). Hence, we hold that, the shear-ordering packing fraction increases with increasing inelasticity, as in the hard-disk system.

The shear-ordered $C_n$ are lower than those of the thermodynamic solid, evident clearly in the $C_2$ data. From Table III we note the following: $C_n$ of the fcc and the hexagonal close-packed (hcp) lattices are nearly identical and the $C_n$ for sheared structures are in between those of the bcc and fcc/hcp lattices, at the same packing fraction. This is indicative of the coexistence of a bcc-like order along with the fcc order in the dense sheared inelastic hard-sphere structures. We discuss this further while analyzing $P_n$ below.

During the plastic deformation of fcc solids ($ABC$ stacking), a close-packed (111) plane slides over another in a zig-

TABLE II. System size dependence check $C_1$ and $C_2$ for inelastic hard spheres sheared in the preferred orientation, for a constant coefficient of restitution $\epsilon=0.70$.

| $\nu$ | Run | $C_1$ | $C_2$ |
|---|---|---|---|
| 0.45 | I[a] | 14.8317 | 59.4936 |
| | II[b] | 14.8335 | 59.5084 |
| | III[c] | 14.8263 | 59.4719 |
| | IV[d] | 14.8270 | 59.4691 |
| 0.50 | I | 14.7323 | 58.5598 |
| | II | 14.7301 | 58.5493 |
| | III | 14.7371 | 58.6100 |
| | IV | 14.7235 | 58.5273 |
| 0.57 | I | 14.0701 | 52.7385 |
| | II | 14.0705 | 52.7770 |
| | III | 14.0942 | 52.8972 |
| | IV | 14.1058 | 53.0466 |
| 0.61 | I | 14.0393 | 52.4071 |
| | II | 14.0336 | 52.4847 |
| | III | 14.0521 | 52.4887 |
| | IV | 14.0594 | 52.5013 |

[a]Averaged for 1200 configurations of 216 (6 stacks of $6\times6$) hard-spheres, $l_x:l_y:l_z=6:6\sqrt{2/3}:6\sqrt{3}/2$.
[b]Averaged for 675 configurations of 384 (6 stacks of $8\times8$) hard-spheres, $l_x:l_y:l_z=8:6\sqrt{2/3}:8\sqrt{3}/2$.
[c]Averaged for 450 configurations of 576 (9 stacks of $8\times8$) hard-spheres, $l_x:l_y:l_z=8:9\sqrt{2/3}:8\sqrt{3}/2$.
[d]Averaged for 288 configurations of 900 (9 stacks of $10\times10$) hard-spheres, $l_x:l_y:l_z=10:9\sqrt{2/3}:10\sqrt{3}/2$.

zag path, alternating between type-$B$ and type-$C$ sites [14]. This phenomenon is noted also in colloidal suspensions [15]. This motion corresponds to the zig-zag haze in the pair distribution function projected on the velocity-vorticity ($xz$) plane, Fig. 11.

In Fig. 12, we present the angular-averaged pair distribution function at contact $g(\sigma)$. For comparison we show that $g(\sigma)$ values for the thermodynamic fluid and solid, computed from the equations of states as

TABLE III. $C_1$ and $C_2$ for different structured systems at $\nu=0.59$.

| System | $C_1$ | $C_2$ |
|---|---|---|
| bcc[a] | 14.0231 | 50.2857 |
| hcp[b] | 14.0687 | 53.7314 |
| fcc[c] | 14.0695 | 53.6867 |
| sheared[d] | 14.0456 | 52.4773 |

[a]Averaged for 1000 configurations of 432 hard spheres, $l_x:l_y:l_z=1:1:1$.
[b]Averaged for 1000 configurations of 384 (6 stacks of $8\times8$) hard spheres, $l_x:l_y:l_z=8:6\sqrt{2/3}:8\sqrt{3}/2$.
[c]Averaged for 1000 configurations of 256 hard spheres, $l_x:l_y:l_z=1:1:1$.
[d]$\epsilon=0.90$, averaged for 675 configurations of 384 hard spheres, $l_x:l_y:l_z=8:6\sqrt{2/3}:8\sqrt{3}/2$.

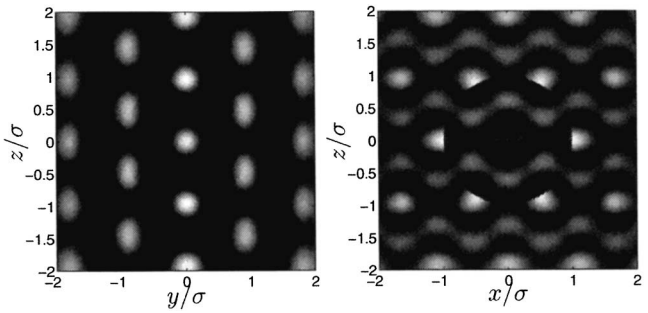


FIG. 11. The pair-distribution function projected on the velocity gradient-vorticity ($yz$) plane and the velocity-vorticity ($xz$) plane, for the preferred orientation shear of inelastic hard spheres at $\nu=0.54$ and $\epsilon=0.99$. Averaged for 5000 configurations of 384 hard spheres, with PBC.

$$g(\sigma)=\frac{Z-1}{B_2\rho}, \tag{13}$$

where $Z=p\bar{v}/(k_BT)$ is the compressibility factor and $B_2=(2/3)\pi\sigma^3$ is the hard-sphere second virial coefficient. For the thermodynamic fluid phase we use the Carnahan-Starling equation [51]

$$Z=\frac{1+\nu+\nu^2-\nu^3}{(1-\nu)^3}. \tag{14}$$

For the thermodynamic solid phase we use the Young-Alder equation [52]

$$Z=\frac{3}{a}+2.566+0.55a-1.19a^2+5.95a^3, \tag{15}$$

where $a=(1-y)/y$ is the fractional free volume and $y=\nu/\nu_c$ is the normalized packing fraction and $\nu_c=\pi/(3\sqrt{2})$ is the regular close-packed packing fraction. Some of the conclusions which we drew from the analysis of $C_n$, can

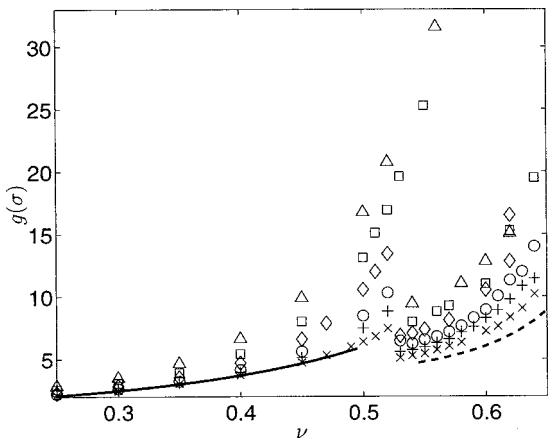


FIG. 12. $g(\sigma)$ for the preferred orientation shear of inelastic hard spheres, at $\epsilon=0.60$ (△), 0.70 (□), 0.80 (◇), 0.90 (○), 0.95 (+), 0.99 (×), compared with Carnahan-Starling equation for the thermodynamic fluid phase (continuous line) and the Young-Alder equation for the solid phase (dashed line). Data sets averaged for 675 configurations of 384 hard spheres, with PBC.

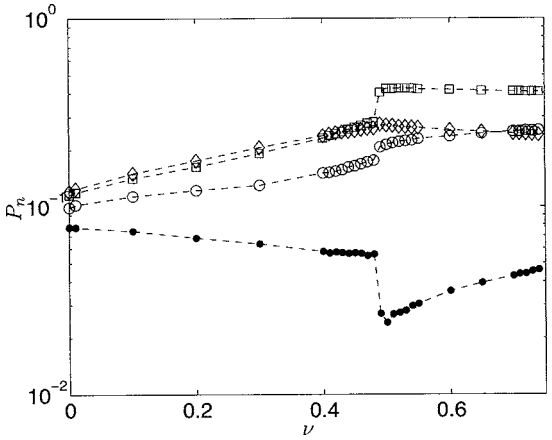


FIG. 13. $P_n$ for hard-sphere NVE configurations, for $n=12$ (•), 13 (◦), 14 (□), and 15 (◇). Averaging as in Fig. 9.

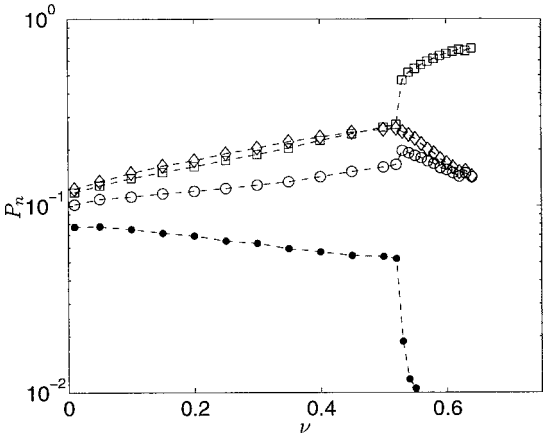


FIG. 15. $P_n$ for sheared inelastic hard-sphere structures at $\epsilon=0.90$, for $n=12$ (•), 13 (◦), 14 (□), and 15 (◇). Averaging as in Fig. 9.

indeed be drawn from $g(\sigma)$ also, for example, the shear ordering transitions and the approach to thermodynamic structures by the near-elastic sheared structures. However, a structural analysis based on $g(\sigma)$ could be misleading, for example, in Fig. 12 the highly inelastic solid structures seem to be a continuation of the thermodynamic fluid phase. But from our analysis of $C_1$ in Fig. 9, we know that such an inference is erroneous. From Voronoi partitioning (Sec. III), note that $g(\sigma)=g_1(\sigma)$ is composed of $C_1$ and $f_1(\sigma)$. As packing fraction increases $C_1$ decreases (except during amorphization, as noted below) and $f_1(\sigma)$ increases. And both $C_1$ and $f_1(\sigma)$ decrease suddenly across an ordering transition. Since $g(\sigma)$ is composed of terms with such mixed trends, structural inferences based on it could be misleading, as shown above. Hence, the $C_n$ are superior structural indices than $g(\sigma)$.

The $P_n$ for thermodynamic and sheared structures are given in Figs. 13–16. Due to the topological instability of the fcc lattice, near the regular close packed limit, the thermodynamic solid has Voronoi polyhedra with faces ranging from 12 to 18 (as observed in Figs. 13 and 14) with a mean at 14, the original proof is outlined in the appendix of our earlier work Ref. [9]. Comparing the $P_n$ of thermodynamic and sheared structures, we see that the 14-faceted polyhedron incidence has increased in the sheared solid phase, at the expense of the 12, 13, 15–18 faceted polyhedra. Due to the depletion of the high-faceted polyhedra, $C_1=\Sigma nP_n$ of the sheared solid structure is lower than that of the thermodynamic solid structure. This effect gets amplified for the second nearest neighbors and hence more prominent in Fig. 10. The Voronoi polyhedron of the bcc lattice is the truncated octahedron, which has six square and eight hexagonal faces, a total of 14 faces. The bcc polyhedron is topological stable to perturbations [53,54], unlike the fcc or hcp polyhedra [19]. From Table IV we note the following: $P_n$ of the fcc and hcp lattices are nearly identical and the $P_n$ for sheared structures are inbetween those of the bcc and fcc/hcp lattices, at the same packing fraction. This high incidence of 14-faceted polyhedron is a clear indication of the presence of a bcc-like structure in dense sheared inelastic hard spheres. During martensitic transformations, a rapidly quenched fcc metallic structure gets sheared to the bct structure, by a mechanism called the Bain distortion [55]. When a cubic lattice (with lattice parameters $a=b=c$) is compressed or stretched in one

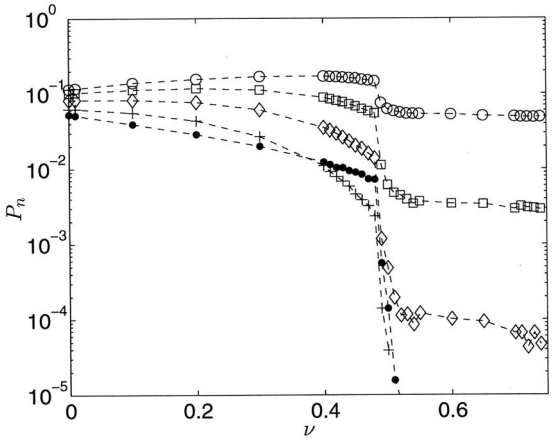


FIG. 14. $P_n$ for hard-sphere NVE configurations, for $n=11$ (•), 16 (◦), 17 (□), 18 (◇), and 19 (+). Averaging as in Fig. 9.

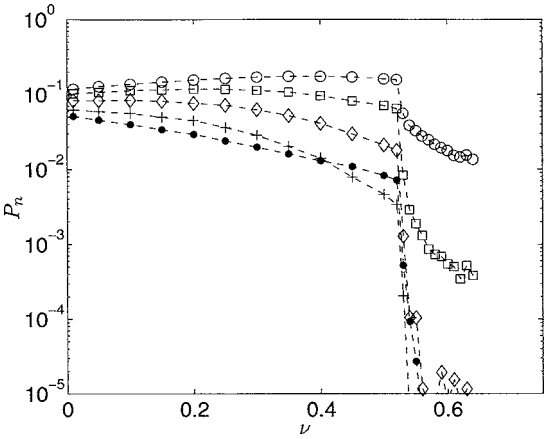


FIG. 16. $P_n$ for sheared inelastic hard-sphere structures at $\epsilon=0.90$, for $n=11$ (•), 16 (◦), 17 (□), 18 (◇), and 19 (+). Averaging as in Fig. 9.

TABLE IV. Percentage distribution of the number of faces of the Voronoi polyhedra for different structured systems at $\nu=0.59$.

| | $P_n \times 100$ | | | |
|---|---|---|---|---|
| $n$ | bcc[a] | hcp[b] | fcc[c] | sheared[d] |
| 12 | 0.01 | 4.03 | 3.44 | 0.68 |
| 13 | 1.89 | 23.65 | 23.44 | 15.96 |
| 14 | 93.95 | 40.76 | 41.83 | 63.56 |
| 15 | 4.07 | 25.07 | 25.66 | 17.80 |
| 16 | 0.07 | 5.95 | 5.28 | 1.93 |
| 17 | 0 | 0.51 | 0.35 | 0.07 |
| 18 | 0 | 0.01 | 0.01 | 0 |

[a]Averaged for 1000 configurations of 432 hard-spheres, $l_x:l_y:l_z=1:1:1$.
[b]Averaged for 1000 configurations of 384 (6 stacks of $8\times8$) hard-spheres, $l_x:l_y:l_z=8:6\sqrt{2/3}:8\sqrt{3}/2$.
[c]Averaged for 1000 configurations of 256 hard-spheres, $l_x:l_y:l_z=1:1:1$.
[d]$\epsilon=0.90$, averaged for 675 configurations of 384 hard-spheres, $l_x:l_y:l_z=8:6\sqrt{2/3}:8\sqrt{3}/2$.

direction it becomes a tetragonal lattice (with lattice parameters $a=b\neq c$). The bct structures similarly formed in the dense homogeneously sheared inelastic hard spheres leave a bcc-like signature in the $C_n$ and $P_n$ data. A detailed bond-orientational analysis of dense sheared microstructures will be reported separately.

Now we consider shear in an unpreferred orientation, with the (001) plane parallel to the velocity-vorticity ($xz$) plane. Since, crystalline solids are anisotropic, their properties vary with direction. Woodcock [16] is critical about the unpreferred orientation shear simulations, and considers the observations as artifacts. However, we consider such simulations as indicative of metastable or transient states, since shearing in an unpreferred orientation the structure melts and (given sufficient time) recrystallizes in the preferred orientation. In Fig. 17 we compare the $C_1$ for the preferred and an unpreferred orientation, from which we observe the following.

For fluid states, the orientation of the initial configuration does not matter, hence the structures are identical for both the preferred and unpreferred orientations.

When the system sheared in an unpreferred orientation, the lattice melts and recrystallizes in the preferred orientation, hence $\nu^u_{\rm ord}\geqslant\nu^p_{\rm ord}$, where $\nu^u_{\rm ord}$ and $\nu^p_{\rm ord}$ are the shear ordering packing fractions in an unpreferred and the preferred orientations. In Fig. 17, $\nu^u_{\rm ord}\approx0.59$ and $\nu^p_{\rm ord}\approx0.53$. In Fig. 18, for $\nu=0.60$ note that the lattice orientation has not stabilized, compare with the lattice orientation in Fig. 11.

In an unpreferred orientation shear, at packing fractions above shear ordering packing fraction, the system gets disordered or amorphized, as observed in Fig. 18. This phenomenon is analogous to the strain-induced amorphization of nanocrystals [20] [in this work also shear is along the (001) plane]. This is a metastable state, because on annealing or given infinite time the sample will recrystallize. While amorphization was absent in the preferred orientation shear, it is observed in an unpreferred orientation shear. We reason its

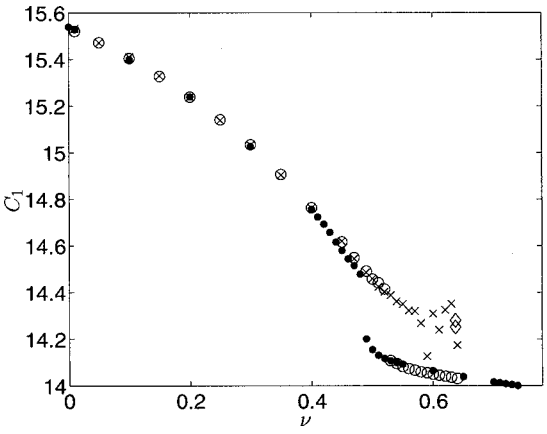


FIG. 17. $C_1$ for sheared inelastic hard-sphere structures at $\epsilon=0.99$, at the preferred (∘) and an unpreferred (×) orientation, compared with NVE structures (•). Averaging as in Fig. 9. The experimental observations by Finney (Ref. [57]) at $\nu_{\rm DRP}\approx0.64$ are (◇).

cause as follows: X-ray diffraction studies show that plastic deformation does not disorder a crystal, even though the defect concentration increases. Most of the plastic deformation is by slipping, in which the particle displacements are along the slip planes. Hence, we infer that if the imposed displacement or velocity lies in a slip plane, the lattice need not break. This corroborates with the fact that amorphization was not observed in the preferred orientation shear (more below). Now, when the imposed displacement or velocity does not lie in a slip plane, it is intuitively obvious that simultaneous shear and slip can break the lattice. We consider this to be a cause for the metastable amorphization in an unpreferred orientation shear. If the relaxation time of the system is very small as compared to the shear, this metastable amorphization will not be observed, since the system will recrystallize quickly in the preferred orientation. In most colloidal system, at higher shear rates shear thickening is observed. A steady state amorphization is considered to be its cause [21,22], and it is observed in Stokesian dynamics simulations [56]. Shear

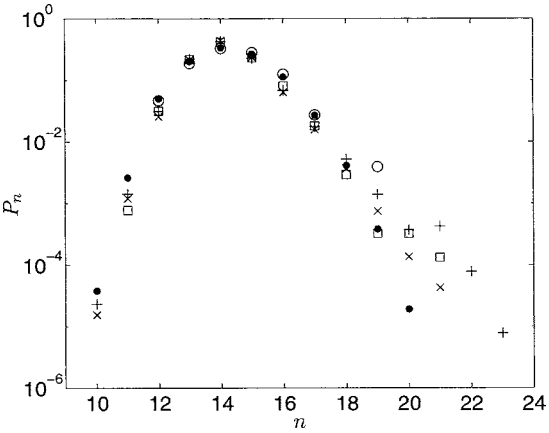


FIG. 18. $P_n$ for inelastic hard-spheres sheared at an unpreferred orientation, at $\nu=0.63$ and $\epsilon=0.99$ for different system sizes [N=256 (∘), 500 (□), 864 (×), and 1372 (+)], compared with the swelled random structures (•).

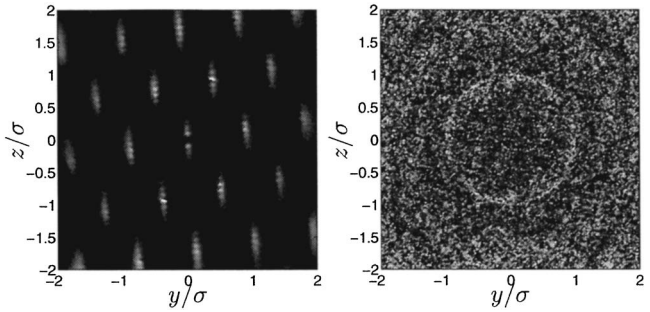


FIG. 19. The pair-distribution function projected on the velocity gradient-vorticity ($yz$) plane for an unpreferred orientation shear of inelastic hard spheres at $\nu=0.60$ and $\nu=0.63$, with $\epsilon=0.99$. Averaged for 5000 configurations of 384 hard spheres, with PBC.

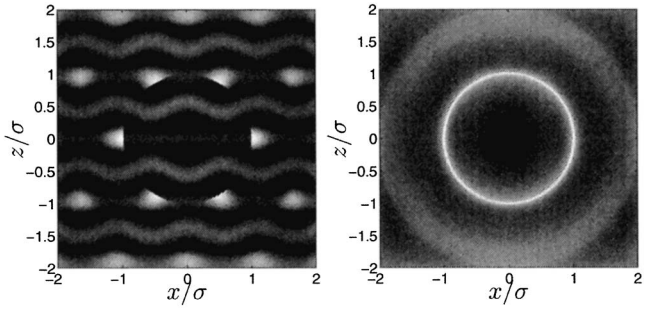


FIG. 20. The pair-distribution function projected on the velocity-vorticity ($xz$) plane for the preferred orientation shear of 20 mm diameter spheres at shear rates $\dot{\gamma}=2400$ and 2500 $s^{-1}$, at $\nu=0.545$ for the velocity dependent COR model. Averaged for 5000 configurations of 384 hard spheres, with PBC.

thickening by amorphization requires that, at a given packing fraction, the structure change with shear rate. Hence, shear-thickening cannot be observed with the constant COR model, for which the structures are shear rate independent. Below we demonstrate that using a velocity-dependent COR steady state amorphization can be realized even in the preferred orientation.

We speculate that for packing fractions well above the dense random packing, an unpreferred orientation shear will break the lattice into polycrystalline structure and over long times the grains will reorient and crystallize in the preferred orientation. Our simulation sizes and times are too small to observe such a phenomenon.

From Fig. 17 we note that the $C_1$ for amorphized structures are close to that reported by Finney [57] for two different experimental realizations of dense random packing, $C_1=14.251\pm0.015$ and $14.28\pm0.05$. Fig. 19 shows that the distribution of the faces of the Voronoi polyhedra ($P_n$) of such structures match reasonably with those of the swelled random structures [9], except for the higher incidence of some high-faceted polyhedra at the expense of the low-faceted ones. Structural relaxation using the swelling algorithm [9] can rectify the same. Thus, the Lees-Edwards boundary condition for nearly elastic hard spheres at $v\approx0.64$, in an unpreferred orientation, followed by a few swelling cycles for structural relaxation, offers a nearly deterministic route to generate dense random packings.

In an unpreferred orientation shear, we find that the shear ordering fraction increases with inelasticity in a wider range than in the preferred orientation, data not shown.

Before we present the simulation results, we demonstrate the possibility of achieving of steady state amorphization in the preferred orientation with the velocity-dependent COR. From Fig. 9, note that shear ordering occurs in the range $\nu=0.52-0.53$ for $\epsilon=0.999-0.8$ and at $\nu\approx0.55$ for $\epsilon=0.70$. Suppose the velocity-dependent COR sheared structures could be related (at least approximately) to that at some constant COR. At $\nu=0.545$, say the shear rate is initially such that the average COR is greater than 0.80, then the system is shear ordered. Now, if the shear rate is increased such that the average COR decreases below 0.70, then the system will get amorphized. Even if the system is globally in preferred orientation, near defects such as edge dislocations or grain boundaries, a $\langle111\rangle$ plane may be locally misoriented and not contain the velocity. Such locations act as nuclei for disorder, since simultaneous shear and slip on such planes will generate more defects. When the local amorphization rate exceeds the local crystallization rate, a steady amorphized state results. In our simulations, at state points just before amorphization, we found more disorder near the top and bottom boundaries of the simulation cell. Probably the top and bottom boundaries of the simulation cell behave as grain boundaries, due to velocity differences among the top, central and bottom boxes.

Ackerson *et al.* [58] have observed shear thickening in suspension of polystyrene latex spheres (0.109 $\mu$m) suspended in density-matched-water–heavy-water mixture at 400 $s^{-1}$ shear rate. Cao and Ahmadi [59] use a constant COR $\epsilon=0.90$ for polystyrene spheres. Since we could not find the velocity-dependent COR data for polystyrene in the literature, we use that of Nylon reported by Labous *et al.* [30], the average COR is $\epsilon=0.97\pm0.03$ for spheres in the range 6.35–25.4 mm, and $v_Y=9$ m/s. Their data fits our COR model Eq. (5), with $B=0.12$ and $C=0.44$. With these material constants, a steady state amorphization is observed in the preferred orientation shear, for 20 mm diameter spheres near a critical shear rate $\dot{\gamma}_c\approx2500$ $s^{-1}$, as seen from the projected pair distribution function in Fig. 20. From the data in Table V, we observe that $\dot{\gamma}_c$ increases with decreasing particle diameter. For shear-thickening dense suspensions $\dot{\gamma}_c\sim\sigma^{-2}$, Refs. [22,60]. However, in our simulations we observe that $\dot{\gamma}_c\sim\sigma^{-1}$, i.e., $\dot{\gamma}_c\sigma\approx$const($\sigma=10$ mm, $\dot{\gamma}_c\approx4900-5000s^{-1}$; $\sigma=15$ mm, $\dot{\gamma}_c\approx3500-3600$ $s^{-1}$; $\sigma=20$ mm, $\dot{\gamma}_c\approx2400-2500$ $s^{-1}$; $\sigma=25$ mm, $\dot{\gamma}_c\approx1900-2000$ $s^{-1}$). The inverse linear proportionality of $\dot{\gamma}_c$ with $\sigma$ is predicted for the shear thickening of granular suspensions by Savage and Jeffreys [23](quoted in Ref. [60]). In our system, at a given packing fraction, $v_Y/(\dot{\gamma}_c\sigma)$ is the only material dimensionless group, and insisting its constancy at amorphization, the above scaling is recovered. Note that the average COR of Nylon is higher than that of polystyrene, hence we require higher shear rates to observe amorphization. We have used sphere diameters for much higher than that of polystyrene (0.109 $\mu$m), in Table V, so that amorphization in observed in the typical range of shear rates (0 to $10^5$ $s^{-1}$). However, note that in colloidal suspension due to the screened electrostatic

TABLE V. Shear amorphization with velocity-dependent COR in the preferred orientation, at $\nu=0.545$ at different sphere diameters. Averaged for 675 configurations of 384 hard spheres (6 stacks of $8\times8$ hard spheres), $l_x:l_y:l_z=8:6\sqrt{2/3}:8\sqrt{3}/2$.

| $\sigma$ mm | $\dot{\gamma}s^{-1}$ | $C_1$ | $C_2$ |
|---|---|---|---|
| 10 | 4800 | 14.0959 | 53.1667 |
| | 4900 | 14.0978 | 53.1682 |
| | 5000 | 14.5478 | 57.1050 |
| | 5200 | 14.5705 | 57.2308 |
| 15 | 3400 | 14.0984 | 53.1841 |
| | 3500 | 14.0953 | 53.1508 |
| | 3600 | 14.5504 | 57.0752 |
| | 3700 | 14.5674 | 57.1976 |
| 20 | 2300 | 14.1024 | 53.1617 |
| | 2400 | 14.0959 | 53.1667 |
| | 2500 | 14.5592 | 57.2328 |
| | 3000 | 14.5627 | 57.1953 |
| 25 | 1800 | 14.0974 | 53.1820 |
| | 1900 | 14.0950 | 53.1631 |
| | 2000 | 14.5478 | 57.1050 |
| | 2200 | 14.5508 | 57.1120 |

interactions (modeled with Yukawa potential [24]), the effective hard-sphere diameter is larger than the actual sphere diameter.

## VI. CONCLUSIONS

Inelastic hard-particles are the simplest model for rapid granular matter. We have generated the homogeneously sheared inelastic hard-disk and hard-sphere structures using the Lees-Edwards boundary condition, and performed a Voronoi neighbor analysis for these structures. In most of the work, we have used the constant coefficient of restitution model for inelastic collisions. Due to the lack of an intrinsic energy scale, the resultant structures are shear rate independent. Hence, to study the shear-dependent structures, we have used a velocity-dependent coefficient of restitution. We propose a functional form for the velocity-dependent coefficient of restitution, Eq. (5), which accommodates both the viscoelastic and the plastic deformation scalings.

In a given configuration, all the spheres surrounding a central sphere are partitioned layerwise, and characterized by $n$th neighbor coordination number ($C_n$) and $n$th neighbor position distribution function [$f_n(\mathbf{r})$]. We have shown that the total information contained in the pair distribution function $g(\mathbf{r})$ can be partitioned into these sets of neighbor statistics. The distribution of the number of Voronoi bounding surfaces ($P_n$) is also of interest, because $C_1$ is its mean. These neighbor statistics are sensitive microstructural changes such as thermodynamic freezing, shear ordering and shear amorphization transitions, and can distinguish thermodynamic, quenched, and sheared structures.

Both the sheared inelastic hard-disk and hard-sphere (in the preferred orientation) structures show the following. In the near-elastic limit these sheared fluid statistics approach that of the thermodynamic fluid values. When these sheared neighbor statistics approach the thermodynamic solid phase values, shear ordering transition takes place. On shear ordering, close-packed layers of particles slide over each other. In colloids and dense suspensions, such a layerwise flow causes shear thinning, since sliding close-packed layers offer lesser resistance to shear than a disordered structure. The Voronoi statistics clearly show the suppression of crystal nucleation by homogeneous shear. As inelasticity increases the shear ordering packing fraction increases. Due to a topological instability, a thermodynamic hard-sphere solid, has polyhedra with faces 12 to 18, with the mean at 14. In shear ordered inelastic hard-sphere structures there is a high incidence of 14-faceted polyhedra and a consequent depletion of polyhedra with faces 12, 13, 15–18, due to the formation of body-centered-tetragonal (bct) structures. These bct structures leave a bcc-like signature in the $C_n$ and $P_n$ data.

In an unpreferred orientation shear, at packing fractions above shear ordering, the structures get amorphized. This is a metastable amorphization, since the system will eventually recrystallize in the preferred orientation. When the imposed displacement or velocity does not lie on a slip plane, simultaneous slip and shear can break the lattice. We consider this as a cause for the metastable amorphization observed in an unpreferred orientation shear. These structures are nearly identical to the dense random structures, except for the higher incidence of some high-faceted polyhedra at the expense of some low-faceted ones. This aberration can be rectified by a structural relaxation using the Monte Carlo based swelled random algorithm [9]. Thus, the Lees-Edwards boundary condition simulation for nearly elastic hard spheres sheared in an unpreferred orientation, followed by a structural relaxation using the swelled random algorithm, offers a nearly deterministic algorithm to generate dense random packings.

A steady state amorphization is the cause of shear thickening observed in dense suspensions. The constant coefficient of restitution sheared structures are shear rate independent, hence they cannot amorphize as shear rate is varied. We have demonstrated a steady state amorphization with a velocity-dependent coefficient of restitution. Even when the system is globally in the preferred orientation, the slip planes are locally misoriented near edge dislocations and grain boundaries. At these locations, shear induces local amorphization, since the velocity does not lie on these local slip planes. When the local amorphization rate exceeds the local recrystallization rate, a steady amorphized state results. We observe that the critical shear rate for amorphization is inversely proportional to the sphere diameter, as predicted by Savage and Jeffreys [23] for granular suspensions, unlike the inverse square scaling observed in the colloidal suspensions.

[1] G. Voronoi, J. Reine Angew. Math. **134**, 198 (1908).
[2] D. C. Rapaport, Mol. Phys. **48**, 23 (1983).
[3] F. Aurenhammer, ACM Comput. Surv. **23**, 345 (1991).
[4] A. Okabe, B. Boots, and K. Sugihara, *Spatial Tessellations: Concepts and Applications of Voronoi Diagrams* (Wiley, New York, 1992).
[5] G. Schliecker, Adv. Phys. **51**, 1319 (2002).
[6] B. N. Boots, Metallography **15**, 53 (1982).
[7] H. X. Zhu, S. M. Thorpe, and A. H. Windle, Philos. Mag. A **81**, 2765 (2001).
[8] L. Oger, A. Gervois, J. P. Troadec, and N. Rivier, Philos. Mag. B **74**, 177 (1996).
[9] V. S. Kumar and V. Kumaran, J. Chem. Phys. **123**, 074502 (2005).
[10] A. W. Lees and S. F. Edwards, J. Phys. C **5**, 1921 (1972).
[11] C. S. Campbell, J. Fluid Mech. **203**, 449 (1989).
[12] E. J. Stancik, G. T. Gavranovic, M. J. O. Widenbrant, A. T. Laschitsch, J. Vermant, and G. G. Fuller, Faraday Discuss. **123**, 145 (2003).
[13] W. D. Callister Jr., *Materials Science and Engineering—An Introduction*, 5th ed. (Wiley, New York, 2000).
[14] A. H. Cottrell, *Dislocations and Plastic Flow in Crystals* (Clarendon, Oxford, 1953).
[15] B. J. Ackerson, J. Rheol. **34**, 553 (1990).
[16] L. V. Woodcock, Phys. Rev. Lett. **54**, 1513 (1985).
[17] S. Butler and P. Harrowell, Phys. Rev. E **52**, 6424 (1995).
[18] R. Blaak, S. Auer, D. Frenkel, and H. Lowen, Phys. Rev. Lett. **93**, 068303 (2004).
[19] J. P. Troadec, A. Gervois, and L. Oger, Europhys. Lett. **42**, 167 (1998).
[20] H. Ikeda, Y. Qi, K. Samwer, W. L. Johnson, and W. A. Goddard III, Phys. Rev. Lett. **82**, 2900 (1999).
[21] R. L. Hoffman, Trans. Soc. Rheol. **16**, 155 (1972).
[22] R. L. Hoffman, J. Rheol. **42**, 111 (1998).
[23] S. B. Savage and D. J. Jeffrey, in *Euromech* (Oxford University Press, Oxford, 1980), Vol. 133.
[24] M. J. Stevens and M. O. Robbins, Phys. Rev. E **48**, 3778 (1993).
[25] I. Goldhirsch and M. L. Tan, Phys. Fluids **8**, 1752 (1996).
[26] S. F. Foerster, M. Y. Louge, H. Chang, and K. Allia, Phys. Fluids **6**, 1108 (1994).
[27] C. V. Raman, Phys. Rev. **12**, 442 (1918).
[28] F. G. Bridges, A. Hatzes, and D. N. C. Lin, Nature (London) **309**, 333 (1984).
[29] K. L. Johnson, *Contact Mechanics* (Cambridge University Press, New York, 1985).
[30] L. Labous, A. D. Rosato, and R. N. Dave, Phys. Rev. E **56**, 5717 (1997).
[31] L. Y. Li, C. Y. Wu, and C. Thornton, J. Mech. Eng. Sci. **216C**, 421 (2002).
[32] H. Hayakawa and H. Kuninaka, Chem. Eng. Sci. **57**, 239 (2002).
[33] G. Kuwabara and K. Kono, Jpn. J. Appl. Phys., Part 1 **26**, 1230 (1987).
[34] T. Poschel and T. Schwager, Phys. Rev. Lett. **80**, 5708 (1998).
[35] T. Schwager and T. Poschel, Phys. Rev. E **57**, 650 (1998).
[36] S. R. Dahl and C. M. Hrenya, Phys. Fluids **16**, 1 (2004).
[37] T. Poschel, N. V. Brilliantov, and T. Schwager, Physica A **325**, 274 (2003).
[38] F. Spahn, U. Schwarz, and J. Kurths, Phys. Rev. Lett. **78**, 1596 (1997).
[39] S. McNamara and E. Falcon, Phys. Rev. E **71**, 031302 (2005).
[40] A. Rahman, J. Chem. Phys. **45**, 2585 (1966).
[41] J. L. Meijering, Philips Res. Rep. **8**, 270 (1953).
[42] R. Collins, J. Phys. C **1**, 1461 (1968).
[43] B. J. Alder and T. E. Wainwright, Phys. Rev. **127**, 359 (1962).
[44] M. Alam and C. M. Hrenya, Phys. Rev. E **63**, 061308 (2001).
[45] D. Deng, A. S. Argon, and S. Yip, Philos. Trans. R. Soc. London, Ser. A **329**, 549 (1989).
[46] T. Kanai, T. Sawada, I. Maki, and K. Kitamura, Jpn. J. Appl. Phys., Part 2 **42**, L655 (2003).
[47] J. Vermant and M. J. Solomon, J. Phys.: Condens. Matter **17**, R187 (2005).
[48] M. P. Allen and D. J. Tildesley, *Computer Simulation of Liquids* (Clarendon, Oxford, 1992).
[49] W. G. Hoover and F. H. Ree, J. Chem. Phys. **49**, 3609 (1968).
[50] R. B. Fuller, *Synergetics - Explorations in the Geometry of Thinking* (Macmillan, New York, 1975).
[51] N. F. Carnahan and K. E. Starling, J. Chem. Phys. **53**, 600 (1970).
[52] D. A. Young and B. J. Alder, J. Chem. Phys. **70**, 473 (1979).
[53] M. Tanemura, Y. Hiwatari, H. Matsuda, T. Ogawa, N. Ogita, and A. Ueda, Prog. Theor. Phys. **58**, 1079 (1977).
[54] C. S. Hsu and A. Rahman, J. Chem. Phys. **71**, 4974 (1979).
[55] Z. Nishiyama, *Martensitic Transformations* (Academic, New York, 1978).
[56] A. Sierou and J. F. Brady, J. Rheol. **46**, 1031 (2002).
[57] J. L. Finney, Proc. R. Soc. London, Ser. A **319**, 479 (1970).
[58] B. J. Ackerson, J. B. Hayter, N. A. Clark, and L. Cotter, J. Chem. Phys. **84**, 2344 (1986).
[59] J. Cao and G. Ahmadi, Int. J. Multiphase Flow **21**, 1203 (1995).
[60] H. A. Barnes, J. Rheol. **33**, 329 (1989).